Biophysical Journal, Volume *114*

Supplemental Information

Highly Disordered Amyloid-β Monomer Probed by Single-Molecule FRET and MD Simulation

Fanjie Meng, Mathias M.J. Bellaiche, Jae-Yeol Kim, Gül H. Zerze, Robert B. Best, and Hoi Sung Chung

SI Materials, Methods, and Theory

Protein expression and incorporation of an unnatural amino acid. The amino acid sequences of Aβ40 and Aβ42 are shown in Fig. 1. For site-specific labeling of the donor (Alexa 488) and acceptor (Alexa 647) dyes, an unnatural amino acid, 4-acetylphenylalanine (Synchem, Elk Grove Village, IL) and a cysteine residue were attached to the N- and C-terminus of Aβ, respectively (UA-Aβ40-C and UA-Aβ42-C). For the incorporation of 4-acetylphenylalanine, we used an amber codon TAG. We prepared two protein constructs for both Aβ40 and Aβ42. To immobilize proteins on a biotin-embedded glass coverslip, a biotin accepting sequence (AviTag, Avidity LLC, Aurora, Colorado) and a flexible linker sequence were attached to the N-terminus of Aβ (Avi-UA-Aβ40-C and Avi-UA-Aβ42-C). The DNA sequences of UA-Aβ42-C and Avi-UA-Aβ42-C are ATGGGTATGAGCTAGGACGCTGAGTTCAGGCACGACTCTGGTTATGAAGTACA CCACCAGAAACTGGTTTTCTTTGCAGAAGATGTAGGTTCAAATAAAGGAGCAATTATTGGCCTG ATGGTGGGTGGTGTCGTGATTGCGTGCTAA and ATGGGTATGAGCGGTCTGAATGATATCTTTG AGGCGCAAAAGATTGAGTGGCACGAGTCCTCCGGTCTGGTCGCGGGTGGTGGCGGCTCTGGCGG CGGCGGCAGCGGTGGCGGCGGCTCGTAGGACGCTGAGTTCAGGCACGACTCTGGTTATGAAGTA CACCACCAGAAACTGGTTTTCTTTGCAGAAGATGTAGGTTCAAATAAAGGAGCAATTATTGGCC TGATGGTGGGTGGTGTCGTGATTGCGTGCTAA, respectively. The codons for unnatural amino acid (TAG), cysteine (TGC) and AviTag are underlined. The DNA sequences of UA-Aβ40-C and Avi-UA-Aβ40-C do not contain the two C-terminal residues (ATTGCG). All four plasmids were constructed by DNA2.0 (DNA2.0, Neward, CA). The pEVOL plasmid (1) encodes an evolved amino acetyl-tRNA synthetase and a suppressor $tRNA_{CUA}$ to incorporate 4-acetylphenylalanine. To ensure the expression of biotinylated proteins, we co-expressed the BirA gene to generate sufficient biotin ligase (Avidity LLC).

We co-transformed *E. coli* strain BL-21 (DE3) (Stratagene, La Jolla, CO) with chloramphenicol-resistant pEVOL, kanamycin-resistant pJ411-BirA, and carbenicillin-resistant pJ414-Aβ, for the expression of Avi-Aβ constructs. For the constructs without AviTag, we co-transformed bacteria with pEVOL and pJ414-Aβ. The expression level of the full-length protein was optimized by varying the ratio of the plasmids because most of the expression was truncated at the TAG site. The optimized condition was 0.6 μL of pEVOL (50 ng/μL), 0.2 μL of pJ411-BirA (50 ng/μL) and 0.2 μL of a protein construct (20 ng/μL). Co-transformed bacteria were spread on LB-agar plates with corresponding antibiotics. After incubation at 37°C overnight, 2 - 3 individual colonies were picked and inoculated in 5 mL LB broth with the same antibiotics combinations for 16-24 hours at 37°C with shaking at 250 rpm. Colonies grown up in liquid medium were diluted into the same medium of 500 - 1000 mL for further growth. After incubation for 6 - 8 hours, expression was induced at OD 0.6 (600 nm) with final concentrations of 1 mM IPTG, 1 mM arabinose, 1 mM 4-acetylphenylalanine and 50 μM *d*-biotin. After overnight incubation at 25°C with shaking at 250 rpm, bacteria was harvested and spun down at 8000 g for 10 minutes using Sorvall LYNX 4000 centrifuge (Thermo Scientific, Waltham, MA). After removing the supernatant, pellets were either used for lysis right away or frozen at - 20°C for future use.

Purification of Aβ40 and Aβ42. Bacteria pellets from 500 mL LB culture were lysed in 20 mL of bacterial protein extraction reagent (B-Per, Thermo Fisher Scientific, Grand Island, NY) with 50 mM benzamidine hydrochloride, 100 μg/mL lysozyme (Sigma, St. Louis, MO), and 5

units of benzonase (Novogen, Madison, WI). The pellets were mixed and re-suspended in the lysis buffer and incubated at room temperature for 30 minutes. The lysate was transferred to 50 mL spinning tubes and centrifuged at 30000 g for 45 minutes with Sorvall LYNX 4000. The supernatant was removed for electrophoresis and the pellet containing inclusion bodies were re-suspended in 30 mL 1× PBS solution with 10 mM DTT and 1% Triton X-100 and sonicated three times for 20 seconds on ice using a sonicator at 100% power (Model Q55, Qsonica, Newtown, CT). The solution was then centrifuged at 30000 g for 30 minutes at 4°C. The supernatant was discarded and the remaining pellet was re-suspended in the same PBS buffer used in the previous sonication step with 1 M sodium chloride to remove DNA and RNA from pellets. The mixture was sonicated as the previous step and centrifuged at 30000 g for 30 minutes at 4°C. Re-suspension, sonication, and centrifugation were repeated in 1× PBS. The pellet containing inclusion bodies was dissolved in 5 mL of 50 mM Tris-HCl with 6 M guanidine hydrochloride (GdmCl) and 10 mM DTT, and kept at room temperature overnight for complete dissolution of proteins. The solution was centrifuged at 30000 g for 45 minutes at 4°C to remove the insoluble pellet and collect the supernatant for further purification. The supernatant was loaded on PhastSystem (Pharmacia, Baltimore, MD) gels. Gels were stained with Phastgel Blue R (Pharmacia, Baltimore, MD) then washed until protein bands were clearly shown. Aβ proteins with and without AviTag and linker appear at 8 kDa and 5 kDa on gels, respectively, and these are the smallest proteins in the inclusion body. 500 μL of protein solutions were loaded onto the AKTA pure FPLC system equipped with a Superdex^{TM}75 10/300GL size exclusion column (GE Healthcare, Chicago, IL). The separation was run with 50 mM Tris-HCl, 4 M GdmCl solution at a flow rate of 0.8 mL/min. The fractions containing 5 kDa or 8 kDa proteins identified by Phastgel were collected and concentrated using Amicon Ultra centrifugal filters (EMD Millipore, Billerica, MA) and then subjected to second round of FPLC purification.

Dye labeling and purification. We first labeled 4-acetylphenylalanine with Alexa Fluor 488 (Alexa 488) hydroxylamine (A30629, Thermo Fisher Scientific, Carlsbad, CA). Aβ (~ 0.2 mg) in 4 M GdmCl solution was exchanged and concentrated to 100 μL in 6 M GdmCl in acetate buffer at pH 4.0 using Amicon centrifugal filters. 100 μL of a protein solution was mixed with 0.1 mg of Alexa 488 hydroxylamine pre-dissolved in 5 μL of DMSO. To promote the reaction, we incubated the mixture at 37°C overnight. The reaction was quenched by adding 4 μL of β-mercaptoethanol and 30 μL of 1 M Tris-HCl, pH 8.0. The reaction mixture was fractionated on a Superdex^{TM}75 10/300GL size exclusion column equilibrated with 50 mM Tris-HCl, pH 8.0, 4 M GdmCl to remove the excess free dye. The fraction containing labeled proteins was concentrated and incubated at room temperature for 1 – 2 hours in the presence of 1.5 mM tris (2-carboxyethyl) phosphine (TCEP) to fully reduce the cysteine residue. TCEP was removed by exchanging buffer into 50 mM Tris-HCl, pH 7.0, 6 M GdmCl and the sample was concentrated to 100 μL. To label cysteine with Alexa Fluor 647 maleimide (Alexa 647, A20347, Thermo Fisher Scientific, Carlsbad, CA), the solution was incubated with 100 μg of Alexa 647 dissolved in 5 μL of DMSO at room temperature overnight. The reaction was quenched by adding 3 μL of β-mercaptoethanol and incubating the solution for 10 minutes. The mixture was loaded onto FPLC and separated with the superdex^{TM}75 10/300GL size exclusion column equilibrated with 50 mM Tris-HCl, pH 8.0, 4 M GdmCl. The peptide labeled with two dyes showed overlapping three peaks of absorbance monitored at 280, 494, and 651 nm. The labeled protein concentration was determined by the absorbance at 494 nm and 651 nm measured by Cary 8454 UV-Vis

spectrophotometer (Agilent Technologies, Santa Clara, CA). Purified samples were aliquoted into 10 μL and kept at - 80°C for future experiments.

Single-molecule experiment. Single-molecule experiments were performed using a confocal microscope system (MicroTime200, Picoquant) with a 75 μm diam. pinhole, a dichroic beamsplitter (ZT405/488/635rpc, Chroma Technology), and an oil-immersion objective (UPLSAPO, NA 1.4, × 100, Olympus). In the free-diffusion experiment, solutions of 40 - 100 pM dye-labeled proteins were prepared in 50 mM 1× PBS, pH 7.5 at various urea concentrations. We added 0.01% Tween-20 to prevent sticking of proteins on a glass coverslip and 100 mM β-mercaptoethanol and 40 mM cysteamine to reduce blinking and bleaching of dyes (2). Alexa 488 was excited by a 485 nm diode laser (LDH-D-C-485, PicoQuant) in the continuous wave (CW) mode at 20 μW. Alexa 488 and Alexa 647 fluorescence was split into two channels using a beamsplitter (585DCXR, Chroma Technology) and focused through optical filters (ET525/50m for Alexa 488 and E600LP for Alexa 647, Chroma Technology) onto photon-counting avalanche photodiodes (SPCM-AQR-16, PerkinElmer Optoelectronics). Photons were collected into 2 ms bins for 1 to 2 hours and those containing 30 photons or more were considered as significant bursts for further analysis.

In the immobilization experiment, Aβ was immobilized on a biotin-embedded, PEG coated glass coverslip (Bio-01, Microsurfaces Inc., Englewood, NJ) as described previously (3). After being cleaned with deionized water and dried with a stream of nitrogen, the surface was covered with Cover well (PC8R-0.5) and pretreated with 20 μL streptavidin solution (25 μg/mL) for 5 minutes. The solution was replaced with 20 μL of 100 pM protein solution and checked on the microscope to monitor binding of proteins on the surface. After observing immobilization of a sufficient number of molecules (50 – 100 molecules per 10 x 10 μm^2), the solution was replaced with 1× PBS including a cocktail of 100 mM β-mercaptoethanol, 10 mM Cystamine, 2 mM 4-nitrobenzyl alcohol (NBA), 2 mM cyclooctatetraene (COT), and 2 mM Trolox (4, 5) to reduce photoblinking and photobleaching of dyes. For the study of the dynamics on the timescale from μs to ms, molecules were illuminated in the CW mode at 3 μW. For the fluorescence lifetime measurement, pulsed-mode excitation was used at the power of 0.3 μW.

All experiments were performed at room temperature (22ºC). Additional details of single-molecule experiments have been described elsewhere (6, 7, 3).

FRET efficiency and donor lifetime corrections in 2D FRET efficiency-lifetime analysis. 2D FRET efficiency-lifetime analysis performed in this study requires accurate values of the FRET efficiency and donor fluorescence lifetime. The mean FRET efficiency and donor delay time of the initial segment of each trajectory were calculated and corrected for various factors (8) including background, donor leak into the acceptor channel (cross-talk), ratio of the detection efficiencies and quantum yields of the donor and acceptor (γ-factor), direct acceptor excitation, and acceptor blinking. Although the details can be found in Ref. (6), we describe the correction procedures below briefly.

FRET efficiency corrections for background, donor leak, and γ-factor. The contribution of background photons is corrected by subtracting the background photon count rates from the mean photon count rates of corresponding detection channels for each segment. The background photon count rates were obtained from the segment after photobleaching of all dyes.

Donor leak into the acceptor channel, l can be measured as

$$l = n_A^0 \big/ (n_A^0 + n_D^0), \tag{S1}$$

where $n_A{}^0$ and $n_D{}^0$ are the background-corrected photon count rates in the acceptor and donor channels of a donor-only segment (no active acceptor). The count rates in the acceptor and donor channels of a segment with acceptor fluorescence are $n_A = n_A{}^c + l n_D{}^c$ and $n_D = (1 - l) n_D{}^c$, respectively, where $n_A{}^c$ and $n_D{}^c$ are the background and donor leak-corrected acceptor and donor count rates. The corrected count rates $n_A{}^c$ and $n_D{}^c$ can be calculated as

$$\begin{aligned} n_D^c &= n_D / (1 - l), \\ n_A^c &= n_A - n_D l / (1 - l) \end{aligned} \tag{S2}$$

The leak value averaged over the available trajectories is $l = 0.05$.

γ is the ratio of the detection efficiencies (η) and quantum yields (ϕ) of the acceptor and donor, $\gamma = (\eta_A \phi_A)/(\eta_D \phi_D)$. This factor can be determined experimentally by comparing the photon count rates of the segments before and after acceptor photobleaching as

$$\gamma = n_A^c \big/ (n_D^0 - n_D^c), \tag{S3}$$

where $n_A{}^c$ and $n_D{}^c$ are the background and donor-leak corrected count rates of the acceptor and donor before acceptor photobleaching and $n_D{}^0$ is that of the donor after acceptor photobleaching. The average γ values are 0.98 and 1.01 for the Aβ40 and Aβ42 experiments, respectively. The γ-corrected FRET efficiency is calculated as

$$E = n_A^c \big/ (n_A^c + \gamma n_D^c). \tag{S4}$$

A small fraction of acceptor count rate results from the direct acceptor excitation because of the weak absorption of the acceptor at the donor excitation wavelength (485 nm). This effect can be corrected together with the γ correction in Eq. S4 by using the γ value determined in Eq. S3 that is calculated from photon count rates including the contribution of direct acceptor excitation as shown in Ref. (6).

Determination and correction of donor fluorescence lifetime. We determined the donor lifetime from the mean donor delay time,

$$\tau_D = \langle \delta t_D \rangle - \delta t_{D0} - \tau_{IRF}^0, \tag{S5}$$

where $\langle \delta t_D \rangle$ is the average time delay of the donor photons from the laser trigger signal, δt_{D0} is the origin of the donor delay time, and τ_{IRF}^0 ($= \int_0^\infty tIRF(t)dt$) is the mean delay time of the

instrument response function (IRF) in the donor channel. IRF was measured using the reflected excitation light from a glass surface and fitted to the Gamma distribution (6, 9),

$$IRF(t) = \frac{k_\gamma}{\Gamma(a)}(k_\gamma t)^{a-1} e^{-k_\gamma t} \quad \text{(S6)}$$

where $\Gamma(a)$ is the Gamma function and a and k_γ are positive fitting parameters. δt_{D0} in Eq. S5 can be obtained by fitting the donor delay time distribution of the donor-only segments (no active acceptor) to the convolution of the IRF and a bi-exponential function as

$$P_D(\delta t) = \int_0^{\delta t} IRF(\delta t - \delta t_{D0} - t)[A_1\tau_1^{-1}\exp(-t/\tau_1) + A_2\tau_2^{-1}\exp(-t/\tau_2)]dt + B_D, \quad \text{(S7)}$$

where constant B_D is the background level in the donor channel. (The details of the calculation of Eq. S7 and fitting can be found in Ref. (6)) The average donor lifetime in the absence of the acceptor ${\tau_D}^0$ obtained by Eq. S5 is 3.1 ns.

Since the donor delay time is not affected by donor leak into the acceptor channel and acceptor direct excitation, it needs to be corrected only for background photons and acceptor blinking (6, 9). The uncorrected mean delay time (τ_D) including the contribution of background photons are related to the corrected mean delay time (${\tau_D}^c$) as $(n_D + b_D)\tau_D = n_D{\tau_D}^c + b_D{\tau_D}^b$, where n_D is the background subtracted donor count rate, b_D and ${\tau_D}^b$ are the background photon count rate and the mean delay time of the background photons in the donor channel. Therefore, the contribution of background photons can be corrected as

$${\tau_D}^c = [(n_D + b_D)\tau_D - b_D{\tau_D}^b] / n_D. \quad \text{(S8)}$$

The correction for acceptor blinking is described in the next section.

Maximum likelihood analysis of acceptor blinking. Donor blinking does not affect the FRET efficiency or lifetime because no photon is detected. However, these quantities are affected by acceptor blinking because only donor photons with long delay times are detected in the acceptor dark state. Since no apparent acceptor blinking is observed in the binned trajectories shown in Figs. 3 and 4, the timescale of the acceptor blinking must be shorter than the bin times. In this section, we describe how to extract acceptor blinking parameters using the maximum likelihood analysis of photon trajectories without binning and correct the FRET efficiency and donor lifetime in the immobilization experiment.

Determination of the acceptor bright state population using two-state maximum likelihood method. The likelihood function for a photon trajectory with records of photon colors and arrival times is (10)

$$L = \mathbf{1}^{\mathrm{T}} \prod_{i=2}^{N} \left[\mathbf{F}(c_i) \exp\left(\mathbf{K}(t_i - t_{i-1})\right) \right] \mathbf{F}(c_1)\mathbf{p}_{eq}, \quad \text{(S9)}$$

where N is the number of photons in a trajectory, c_i is the color of the i^{th} photon (donor or acceptor), and t_i - t_{i-1} is a time interval between the $(i\text{-}1)^{th}$ and i^{th} photons. **K** is the rate matrix, the photon color matrix **F** depends on the color c of a photon as **F**(*acceptor*) = **E** and **F**(*donor*) = **I** – **E**, where **E** is a diagonal matrix with the uncorrected FRET efficiencies of the individual states on the diagonal, **I** is the unity matrix, $\mathbf{1}^T$ is the unit row vector (T means transpose), and $\mathbf{p}_{eq}$ is the vector of equilibrium populations. The parameters were determined by maximizing the likelihood function calculated by the diagonalization of **K** in Eq. S10 as described in Ref. (10).

For the two-state model, the matrix of FRET efficiencies, the rate matrix, and the vector of the equilibrium populations are given by

$$\boldsymbol{E} = \begin{pmatrix} E_1 & 0 \\ 0 & E_2 \end{pmatrix},\ \mathbf{K} = \begin{pmatrix} -k_1 & k_2 \\ k_1 & -k_2 \end{pmatrix},\ \mathbf{p}_{eq} = \begin{pmatrix} p_1 \\ 1-p_1 \end{pmatrix}, \tag{S10}$$

where k_1 (k_2) is the rate coefficient for the transition from state 1 to state 2 (state 2 to state 1) and $p_1 = k_2/(k_1 + k_2)$ is the equilibrium population of state 1. E_1 and E_2 are the apparent FRET efficiencies of state 1 and 2, respectively. The apparent FRET efficiency is the ratio of the acceptor count rate to the total count rate (including background photons). We performed the analysis with two different models. In the 2-state model without constraints in the FRET efficiency, there are four fitting parameters: E_1, E_2, k (= $k_1 + k_2$), and p_1. On the other hand, in the 1-state model with acceptor blinking, state 1 and 2 correspond to the bright and dark states of the acceptor, respectively. We define $k_1 = k_d$, $k_2 = k_b$, $p_1 = p_b$, $E_1 = E_b^{app}$, and $E_2 = E_d^{app}$. In this model, there are three fitting parameters: E_b^{app}, k_b, p_b. The FRET efficiency in the acceptor dark state E_d^{app} was fixed to be 0.06.

In the analysis of the data to probe potential dynamics on the μs – ms timescale (Fig. 3), parameters were extracted from the collective analysis of the entire data set instead of individual trajectories because the length of trajectories is much shorter than those for the 2D FRET efficiency-lifetime analysis due to the 10 times higher illumination intensity. In this case, when using the 1-state model with acceptor blinking, it is reasonable to assume that the rate coefficient for the transition from the bright state to the dark state of the acceptor, k_d, is proportional to the photon count rate while k_b is independent of the photon count rate because k_d increases linearly with the time spent in the excited state. Therefore, $k_d = k_d^0(n/n_0)$, where n is the average photon count rate of each photon trajectory and k_d^0 is the rate coefficient at the reference photon count rate (n_0 = 100 ms^{-1}). The bright state population is $p_b = k_b/(k_b + k_d)$. The parameters extracted using the 2-state model without constraints in the FRET efficiency and the 1-state model with acceptor blinking with a fixed E_d^{app} are compared in Table S2.

In the 2D FRET efficiency-lifetime analysis of the data collected at lower illumination intensity, each trajectory was corrected for acceptor blinking using the 1-state model with acceptor blinking (Fig. 4). In the acceptor dark state, photons are still detected in the acceptor channel because of donor leak and background noise; therefore, the uncorrected count rate in the acceptor channel is $(n - b_A - b_D)l + b_A$, where n is the uncorrected total photon count rate, b_A and b_D are the acceptor and donor background count rates, and l is the donor leak. Since the individual trajectories were analyzed separately, E_d^{app} was calculated for each trajectory to account for the slightly different background level as $E_d^{app} = [(n - b_A - b_D)l + b_A]/n$ and used in

Eq. S10. Fig. S1 *C* shows the bright state population p_b is ~ 0.95. Once p_b is determined for each segment, this value can be used to correct the FRET efficiency and mean donor delay time (lifetime) of each trajectory as described below.

FRET efficiency and lifetime corrections for acceptor blinking. The measured FRET efficiency (corrected for the γ-factor, Eq. S4) is $E = n_A/(n_A + \gamma n_D)$. The acceptor and donor count rates in the presence of acceptor blinking, n_A and n_D, can be expressed in terms of the acceptor bright state population p_b and the FRET efficiency when the acceptor is in the bright state, E^c, as follows. Since acceptor photons are emitted only when the acceptor is in the bright state, the acceptor photon count rate is $n_A = \gamma p_b n E^c$, where n is the background- and donor leak-corrected donor count rate in the absence of the energy transfer. Similarly, the donor count rate in the presence of the acceptor is $n_D = p_b n(1 - E^c) + (1 - p_b)n$, since donor photons are emitted from both bright and dark states of the acceptor. (We assume that there is no energy transfer from the donor to the acceptor in the acceptor dark state.) Using the above expressions for the count rates, we find that $E = p_b E^c$. Therefore, the FRET efficiency can be corrected for acceptor blinking by

$$E^c = E / p_b. \tag{S11}$$

The donor lifetime in the presence of acceptor blinking (τ_D) is the average of the donor lifetimes in the acceptor bright state ($\tau_D{}^c$) and dark state ($\tau_D{}^0$, donor lifetime in the absence of the acceptor) weighted by the donor count rate in each state as $[(1 - E^c)\, p_b + (1 - p_b)]n\,\tau_D = p_b n(1 - E^c)\,\tau_D{}^c + (1 - p_b)n\,\tau_D{}^0$. Note that τ_D is the background-corrected donor lifetime in Eq. S8. Then, the donor lifetime is corrected for acceptor blinking as

$$\tau_D{}^c = \frac{(1-p_b E^c)\tau_D - (1-p_b)\tau_D^0}{p_b(1-E^c)}. \tag{S12}$$

FRET efficiency correction of free-diffusion data. To compare with the values obtained in the immobilization experiment, the FRET efficiency in the free-diffusion experiment was similarly corrected for background, donor leak, and γ-factor.

The FRET efficiency can be corrected for background photons as (8)

$$E = \frac{E^{app} n - b_A}{n - b_A - b_D}. \tag{S13}$$

Here, E^{app} is the apparent FRET efficiency obtained from the FRET efficiency distribution in Fig. 2, n is the average total photon count rate of fluorescence bursts including background photons, and b_A and b_D are the background count rates in the acceptor and donor channels, respectively. In order to obtain b_A and b_D, histograms of photon counts per 2 ms bin were constructed using the entire data set (not just fluorescence bursts) and the low count rate part (< 2 - 3 ms^{-1}) were fitted to the Poisson distribution. The background photon count rates were 0.3 – 0.5 ms^{-1} for both acceptor and donor channels.

The donor leak and γ-factor were corrected using l and γ values obtained from the immobilization experiment. The FRET efficiency values before and after the donor leak correction are $E = n_A/(n_A + n_D)$ and $E^c = n_A{}^c/(n_A{}^c + n_D{}^c)$, respectively. Using the relationship of the photon count rates in Eq. S2, one can correct the donor leak as

$$E^c = \frac{E - l}{1 - l}. \tag{S14}$$

Similarly, γ-factor can be corrected using the relationship between the FRET efficiency before and after the correction as

$$E^c = \left(1 + \gamma\left(1/E - 1\right)\right)^{-1}. \tag{S15}$$

In Eq. S15, E is the FRET efficiency after the donor leak correction in Eq. S14.

Nanosecond fluorescence correlation spectroscopy (nsFCS). In the nsFCS experiments of Avi-Aβ40 and Avi-Aβ42, data were collected in the free-diffusion experiment mode described above at the protein concentration of 1 nM for 10 hours. Fluorescence emission was split by a 50/50 beamsplitter cube and donor and acceptor photons were further separated. The donor and acceptor auto-correlations and donor-acceptor cross correlation were obtained by constructing histograms of time intervals between all pairs of photons detected in different channels as described in Ref. (11, 12). The three correlation data from -2 to 2 μs were globally fitted to

$$C_{ij}(\tau) = A_{ij}(1 - c_{AB}e^{-\tau/\tau_{AB}})(1 + c_{CD}e^{-\tau/\tau_{CD}})(1 + c_T e^{-\tau/\tau_T}), \quad i, j = A, D, \tag{S16a}$$

$$c_{CD} = \begin{cases} \dfrac{\langle n_D^2\rangle - \langle n_D\rangle^2}{\langle n_D\rangle^2} = \dfrac{\sigma_c{}^2}{E^2}, & \text{donor autocorrelation} \\ \dfrac{\langle n_A^2\rangle - \langle n_A\rangle^2}{\langle n_A\rangle^2} = \dfrac{\sigma_c{}^2}{\left(1-E\right)^2}, & \text{acceptor autocorrelation} \\ \dfrac{\langle n_D n_A\rangle - \langle n_D\rangle\langle n_A\rangle}{\langle n_D\rangle\langle n_A\rangle} = -\dfrac{\sigma_c{}^2}{E\left(1-E\right)}, & \text{cross-correlation} \end{cases}. \tag{S16b}$$

Here, A_{ij} is a normalization factor, τ_{AB}, τ_{CD}, and τ_T are the decay times by photon anti-bunching, conformational dynamics, and triplet blinking, respectively, and c_{AB}, c_{CD}, and c_T are the amplitudes of the corresponding components. n_A and n_D in Eq. S16b are acceptor and donor count rates and $\langle\ldots\rangle$ denotes an average over the conformational distribution. E is the true FRET efficiency after all corrections. The variance of the FRET efficiency distribution $\sigma_c{}^2$ can be obtained by globally fitting three correlation functions using the correlation amplitudes of the conformational dynamics c_{CD} in Eq. S16b (13, 3).

Correlation analysis of immobilization data. A donor-acceptor cross-correlation function of the data from the immobilization experiment was calculated as

$$C_{DA}(\tau) = \frac{\overline{\langle N_D(t+\tau)N_A(t)\rangle}}{\langle N_D\rangle\langle N_A\rangle} - 1 . \qquad \text{(S17)}$$

N_D (t) and N_A (t) are the number of donor and acceptor photons in a bin at time t, $\langle\ldots\rangle$ is an average of a quantity in a given segment in a trajectory, and the upper bar indicates the average over segments. The correlation functions in Fig. 3C were calculated for the segments longer than 5 ms.

MD simulations. For each Aβ isoform, we ran temperature replica exchange molecular dynamics (T-REMD) simulations under isobaric-isothermal constraints using both the Amber ff03ws and Amber ff99SBws force fields (14), for 750 ns (Amber ff03ws), 743.760 ns (Amber ff99SBws, Aβ40) or 740.715 ns (Amber ff99SBws, Aβ42) using Gromacs version 4.6.7 (15). 40 temperature windows were used, ranging from T = 277 K to 355 K in steps of ΔT = 2 K, with swaps attempted between adjacent windows every 1 ps. Each system was explicitly solvated with TIP4P/2005 water (16) and 20 mM NaCl plus neutralizing cations.

Forces were evaluated every 2 fs using stochastic dynamics, propagated by integrating the Langevin equation of motion with a friction coefficient of 0.2 ps^{-1}. Isobaric constraints were imposed by using an isotropic Parrinello-Rahman barostat with coupling time constant 5 ps, reference pressure of 1 bar and compressibility 4.5×10^{-5} bar^{-1}, that of water. Nearest neighbor searches were of grid type, using a group cutoff scheme with update frequency of 10 steps and a neighbor list cutoff of 0.9 nm. Nonbonded interactions were treated with a twin range cutoff scheme, with cutoff distances 1.4 nm for van der Waals energies and 0.9 nm for Coulombic energies. Long-range electrostatics were evaluated using a fourth-order particle mesh Ewald sum of spacing 0.12 nm^{-1} with relative tolerance 1×10^{-5}. All bonds were constrained with the LINCS algorithm, and cubic periodic boxes of size (L_x, L_y, L_z) = (5.5, 5.5, 5.5) nm were used as the simulation cell (17–20).

In addition to the REMD simulations, we also performed long simulations with explicit chromophores attached to the peptides. These simulations utilized the Amber ff99SBws force field for the protein, and the Amber-Dyes force field (21) for the chromophores. One minor and likely inconsequential correction was made to the force field: the maleimide-thiol conjugates in the original force field had an incorrect structure (the carbon-carbon double bond was retained in the product). A corrected version of the force field and scripts to add the chromophores to an existing protein structure are available from http://www.github.com/bestlab.

In all analyses shown, frames in which the peptides were within 4.5 Å of their periodic image were discarded to remove unphysical configurations. We discarded the first 375 ns of the trajectories as conformational equilibration (see Fig. S10 *E* and *F*), and time-series of the relevant measurements were generated every 50 ps.

Geometric and *E* analysis. Time-series of the radius of gyration R_g and end-to-end distance R_{ee} were calculated using respectively the `g_gyrate` and `g_dist` utilities of Gromacs. We took R_{ee} as the distance between Cα atoms of the N- and C-termini. Time-series of the FRET

efficiency were generated by conversion of the R_{ee} time-series according to the following equation:

$$E(t) = \frac{1}{1 + \left(R'_{ee}(t) / R_0 \right)^6}, \tag{S18}$$

where we accounted for the effects of the experimental dyes by treating them as 12 extra amino acid residues and assuming a Gaussian scaling exponent (22):

$$R'_{ee}(t) = R_{ee}(t) \left(\frac{N+12}{N} \right)^{0.5}, \tag{S19}$$

where N is either 40 or 42, depending on the peptide isoform.

Time-series of the hydrodynamic radius R_H were generated using the program Hydropro (23) every 50 ps. Specifically, a shell-method calculation was run with the radius of primary elements equal to a = 0.29 nm, with three minibead iterations running from minibead radii σ = 0.1 to 0.2 nm. The temperature was taken to be 25.85°C, the solvent viscosity 0.01 Poise, the solvent density 1.0 gcm^{-3}, the partial specific volume of the peptide 0.741 cm^3g^{-1} and a molecular weight of the peptide equal to 4329.9 Da (Aβ40) or 4514.1 Da (Aβ42). The resultant translational diffusion constants were then transformed to hydrodynamic radii using the Stokes-Einstein equation with a temperature of 299 K and a solvent viscosity of 0.01 Poise.

Averages of all quantities were calculated and errors generated using block averaging with 10 blocks, with the results for R_g, R_{ee}, and E shown in Figs. 6 and S2 for respectively the Amber ff99SBws and Amber ff03ws force fields. For the hydrodynamic radius, these block errors were combined in quadrature with an assumed systematic error of 5% in estimating the diffusion constant (23).

Contact and cluster analysis. Time-dependent inter-residue distance matrices were calculated from non-hydrogen atoms using `g_mdmat` every 50 ps, and converted to contact probability maps $C(t)$ using the continuous transformation:

$$C_{ij}(t) = \frac{1}{1 + \exp\left[\beta \left(r_{ij}(t) - r_0 \right) \right]}, \tag{S20}$$

with β = 500 nm^{-1} and r_0 = 4.5 Å.

Time-averaged contact probability maps $\langle C \rangle_t$ for all simulations were generated by directly counting the fraction of frames in which residues i and j were within 4.5 Å of each other.

To extract the conformational ensemble, we performed a clustering analysis using the k-means algorithm as implemented in the `scipy.cluster.vq` module, with our raw data being the intramolecular contact maps $C(t)$ ignoring all (i, i), (i, i+1), (i, i+2), (i, i+3) and (i, i+4) contacts in order to extract long-range contact information about the peptide ensembles. Note that the

number of clusters allowed by the data is constrained above by $k_{\max} = \left\lfloor \frac{2N_{\text{frames}}}{N_{\text{res}}^2 - 9N_{\text{res}} + 20} \right\rfloor$, where N_{frames} is the number of acceptable (i.e., without periodic contact) frames analyzed, and N_{res} is the length of the peptide primary sequence (i.e., either 40 or 42). This limit comes because in any data fitting problem, the number of fit parameters cannot exceed the number of data points. In these analyses, the number of fit parameters is the number of unique intra-residue contact probabilities (excluding up to and including i to i+4 contacts) multiplied by the number of clusters k: $N_{\text{fit}} = k[N_{\text{res}}(N_{\text{res}} + 1)/2 - 5N_{\text{res}} + 10]$. The number of data points is the number of frames analyzed, as each frame is one possible intra-peptide correlation: $N_{\text{data}} = N_{\text{frames}}$. Equating the two $N_{\text{fit}} = N_{\text{data}}$ so as just to avoid overfitting gives the constraint. Inserting the relevant values gives $k_{\max}$ = 11 (10) and 11 (11) respectively for Aβ40 (Aβ42) using the Amber ff99SBws and Amber ff03ws force fields. At this upper limit, however, each fit parameter is only constrained by one data point; to avoid such overfitting we tried clustering for values of k until only k = 7, when each fit parameter is constrained by approximately 1.5 data points.

We determined that three clusters were enough to describe the average data in all cases except for the Aβ42 Amber ff03ws trajectory, which needed four clusters. The manner in which we decided the appropriate number of clusters was to construct the metric $\Delta = \|\langle C\rangle_t, \langle C\rangle_k\|$, which measures the L_2 distance between the contact map constructed by averaging the contact maps at every time $\langle C\rangle_t$ and the contact map constructing by taking an average of the contact maps of the frames closest to the cluster centers (in contact map space) determined by the algorithm, weighed by the population of each cluster, or $\langle C\rangle_k$. As shown in Fig. S5, this metric is generally decreasing with increasing k, but to avoid over-fitting the data we imposed a cutoff in the fractional decrease in Δ of 10%, which we believe balances the need to describe sufficiently the ensemble against the risk of over-fitting. The contact maps shown in Figs. 7 and S9 are the average contact maps of all frames assigned to each cluster, and the structures shown are those frames that were closest to the determined cluster centers.

To test for the robustness of our clustering analysis, as the k-means algorithm is ultimately stochastic, we repeated the same clustering procedure a second time for both Aβ isoforms, for each of the Amber ff99SBws and ff03ws force fields, with the results summarized in Table S4. In this table, $p_k(\in 2 \mid \in 1)$ is the conditional probabilities that if a frame were assigned to cluster k the first time, it would be assigned to the same cluster the second, and $p_k(\in 1 \mid \in 2)$ the reverse probability. The last column $\|C_1, C_2\|_k$ is the L_2 distance between the average contact maps of the kth cluster generated from the first and second times. As can be seen, there is an extremely high degree of reproducibility in frame assignments, as demonstrated by the near-unity values of the conditional probabilities and the small distances between average contact maps for the same cluster, implying that our clustering was robust. For a sense of scale, the (unitless) distance between the average contact maps of the two major clusters for Aβ40 in the ff99SBws force field is 1.726, and the distance between the most-populated and least-populated clusters is 6.046.

The residue-specific average β-sheet likelihood for each cluster was calculated using the DSSP algorithm (24) as implemented in the `do_dssp` algorithm of Gromacs as the fraction of frames in which each residue was assigned to be in the β-sheet conformation, and the excess β-sheet likelihood of each residue in each cluster was defined as the difference between this β-

sheet likelihood and the ensemble-averaged β-sheet likelihood per residue. Results are shown in Fig. S6 *A*.

NMR analysis. Dihedral angle ($\phi_i(t)$, $\psi_i(t)$) trajectories for each non-terminal residue at 277 K were generated using `g_rama`, and these were converted to residue-specific ${}^3J_{\mathrm{HNH}\alpha}(i)$ coupling constants using the Karplus equation:

$$ {}^3J_{\mathrm{HNH}\alpha}(i,t) = A\cos^2(\phi_i(t) - 60°) + B\cos(\phi_i(t) - 60°) + C\,, \qquad \text{(S21)} $$

with A, B and C parameters taken from (25) as A = 7.97 Hz, B = - 1.26 Hz and C = 0.63 Hz. The coupling constants were then time-averaged and errors were taken as a combination in quadrature of simulation errors by block averaging with 10 blocks and modelling errors due to uncertainties in the determination of the Karplus parameters:

$$ (\Delta {}^3J_{\mathrm{HNH}\alpha}(i))^2 = (\Delta_{\mathrm{block}})^2 + (\Delta_{\mathrm{Karplus}})^2\,, \qquad \text{(S22)} $$

where we estimated the Karplus error term $\Delta_{\mathrm{Karplus}}$ = 0.42 Hz, the RMSD of fitting experimental data in (25).

These coupling constants were then compared against experimentally determined coupling constants as published in (26) to validate our force fields, with the results shown in Figs. 6 and S9. For comparison we use the reduced χ^2, defined as

$$ \chi^2 = \frac{1}{N}\sum_{i=1}^{N}\frac{\left(J_{\mathrm{expt}}(i) - J_{\mathrm{sim}}(i)\right)^2}{\left(\Delta J(i)\right)^2}\,, \qquad \text{(S23)} $$

in which $J_{\mathrm{expt}}(i)$, $J_{\mathrm{sim}}(i)$ and $\Delta J(i)$ are respectively the experimental value, simulation value and estimated error (Eq. S22) for scalar coupling i.

Calculation of chemical shifts. Secondary chemical shift deviations with respect to the random coil are calculated as follows: $\Delta\delta C\alpha = (\delta C\alpha_{\mathrm{sim}} - \delta C\alpha_{\mathrm{ref}})$ and $\Delta\delta C' = (\delta C'_{\mathrm{sim}} - \delta C'_{\mathrm{ref}})$, where $\delta C\alpha_{\mathrm{sim}}$ and $\delta C'_{\mathrm{sim}}$ are predicted Cα and C′ chemical shifts from simulation ensembles using an empirical chemical shift deviation prediction algorithm, SPARTA+ (27). $\delta C\alpha_{\mathrm{ref}}$ and $\delta C'_{\mathrm{ref}}$ respectively are the calculated Cα and C′ random coil reference chemical shifts computed using the Poulsen IDP/IUP random coil chemical shifts calculator at 277 K and pH 7 (28, 29). Errors are predicted by standard block averaging using 10 equal non-overlapping blocks of the data. Results are shown in Fig. S4.

Internal peptide scalings. To obtain information on the relevant intramolecular interactions, we performed a scaling analysis of both isoforms using polymer theory. Namely, we calculated the average inter-Cα atom distance between all residue as a function of sequence separation $|i-j|$ using `g_traj`. Assuming Flory-like behavior, then, these distances should follow a power law:

$$\langle r_{|i-j|} \rangle = b|i-j|^{\nu}, \quad \text{(S23)}$$

where b is the effective length of uncorrelated segments and ν is the scaling exponent, which contains information on the interactions between monomers. The averaging brackets are taken over the inter-residue time-series and over all amino acids $|i-j|$ away from each other in the primary structure. Errors were calculated by block averaging using 10 blocks, and a linear fit of $\ln \langle r_{|i-j|} \rangle$ vs. $\ln |i-j|$, weighted by each point's relative block error, yielded ν, using the standard $b = 0.55$ nm (30). In practice, we fit distances only for $|i-j| \geq 10$, so as not to include the effects of short-range backbone rigidity.

The results are shown in Figs. 7 and S9 respectively for the Amber ff99SBws and Amber ff03ws force fields, and show that both Aβ40 and Aβ42 follow extremely similar short-range behavior, but diverge at long ranges, where the shorter peptide is more expanded than the longer, indicating that long-range attractive contacts account for the observed slight collapse of Aβ42, or that long-range repulsive interactions expand Aβ40. The values of the scaling exponents are around 0.5, as expected for IDP's at or near the Θ-point.

References

1. Young, T.S., I. Ahmad, J.A. Yin, and P.G. Schultz. 2010. An enhanced system for unnatural amino acid mutagenesis in E. coli. *J Mol Biol*. 395: 361–374.
2. Nettels, D., S. Müller-Späth, F. Küster, H. Hofmann, D. Haenni, S. Rüegger, L. Reymond, A. Hoffmann, J. Kubelka, B. Heinz, K. Gast, R.B. Best, and B. Schuler. 2009. Single-molecule spectroscopy of the temperature-induced collapse of unfolded proteins. *Proc Natl Acad Sci U S A*. 106: 20740–20745.
3. Chung, H.S., J.M. Louis, and W.A. Eaton. 2009. Experimental determination of upper bound for transition path times in protein folding from single-molecule photon-by-photon trajectories. *Proc Natl Acad Sci U S A*. 106: 11837–11844.
4. Zheng, Q., S. Jockusch, Z. Zhou, and S.C. Blanchard. 2014. The contribution of reactive oxygen species to the photobleaching of organic fluorophores. *Photochem Photobiol*. 90: 448–454.
5. Zheng, Q., M.F. Juette, S. Jockusch, M.R. Wasserman, Z. Zhou, R.B. Altman, and S.C. Blanchard. 2014. Ultra-stable organic fluorophores for single-molecule research. *Chem Soc Rev*. 43: 1044–1056.
6. Chung, H.S., F. Meng, J.-Y. Kim, K. McHale, I. V. Gopich, and J.M. Louis. 2017. Oligomerization of the tetramerization domain of p53 probed by two- and three-color single-molecule FRET. *Proc Natl Acad Sci U S A*. 114: E6812–E6821.
7. Merchant, K.A., R.B. Best, J.M. Louis, I. V Gopich, and W.A. Eaton. 2007. Characterizing the unfolded states of proteins using single-molecule FRET spectroscopy and molecular simulations. *Proc Natl Acad Sci U S A*. 104: 1528–1533.
8. Gopich, I. V., and A. Szabo. 2012. Theory of single-molecule FRET efficiency histograms. *Adv Chem Phys*. 146: 245–297.
9. Chung, H.S., J.M. Louis, and I. V. Gopich. 2016. Analysis of fluorescence lifetime and energy transfer efficiency in single-molecule photon trajectories of fast-folding proteins. *J Phys Chem B*. 120: 680–699.
10. Gopich, I. V, and A. Szabo. 2009. Decoding the pattern of photon colors in single-molecule FRET. *J Phys Chem B*. 113: 10965–10973.
11. Soranno, A., B. Buchli, D. Nettels, R.R. Cheng, S. Müller-Späth, S.H. Pfeil, A. Hoffmann, E.A. Lipman, D.E. Makarov, and B. Schuler. 2012. Quantifying internal friction in unfolded and intrinsically disordered proteins with single-molecule spectroscopy. *Proc Natl Acad Sci U S A*. 109: 17800–17806.
12. Nettels, D., I. V Gopich, A. Hoffmann, and B. Schuler. 2007. Ultrafast dynamics of protein collapse from single-molecule photon statistics. *Proc Natl Acad Sci U S A*. 104: 2655–2660.
13. Gopich, I. V, D. Nettels, B. Schuler, and A. Szabo. 2009. Protein dynamics from single-molecule fluorescence intensity correlation functions. *J Chem Phys*. 131: 95102.
14. Best, R.B., W. Zheng, and J. Mittal. 2014. Balanced protein–water interactions improve properties of disordered proteins and non-specific protein association. *J Chem Theory*

Comput. 10: 5113–5124.

15. Páll, S., M.J. Abraham, C. Kutzner, B. Hess, and E. Lindahl. 2015. Tackling Exascale Software Challenges in Molecular Dynamics Simulations with GROMACS. In: Lecture Notes in Computer Science (including subseries Lecture Notes in Artificial Intelligence and Lecture Notes in Bioinformatics). . pp. 3–27.
16. Abascal, J.L.F., and C. Vega. 2005. A general purpose model for the condensed phases of water: TIP4P/2005. *J Chem Phys*. 123: 234505.
17. Parrinello, M., and A. Rahman. 1981. Polymorphic transitions in single crystals: A new molecular dynamics method. *J Appl Phys*. 52: 7182–7190.
18. Nosé, S., and M.L. Klein. 1983. Constant pressure molecular dynamics for molecular systems. *Mol Phys*. 50: 1055–1076.
19. Essmann, U., L. Perera, M.L. Berkowitz, T. Darden, H. Lee, and L.G. Pedersen. 1995. A smooth particle mesh Ewald method. *J Chem Phys*. 103: 8577–8593.
20. Hess, B., H. Bekker, H.J.C. Berendsen, and J.G.E.M. Fraaije. 1997. LINCS: A linear constraint solver for molecular simulations. *J Comput Chem*. 18: 1463–1472.
21. Graen, T., M. Hoefling, and H. Grubmüller. 2014. AMBER-DYES: Characterization of Charge Fluctuations and Force Field Parameterization of Fluorescent Dyes for Molecular Dynamics Simulations. *J Chem Theory Comput*. 10: 5505–5512.
22. Zheng, W., A. Borgia, K. Buholzer, A. Grishaev, B. Schuler, and R.B. Best. 2016. Probing the action of chemical denaturant on an intrinsically disordered protein by simulation and experiment. *J Am Chem Soc*. 138: 11702–11713.
23. Ortega, A., D. Amorós, and J. García De La Torre. 2011. Prediction of hydrodynamic and other solution properties of rigid proteins from atomic- and residue-level models. *Biophys J*. 101: 892–898.
24. Kabsch, W., and C. Sander. 1983. Dictionary of protein secondary structure: Pattern recognition of hydrogen bonded and geometrical features. *Biopolymers*. 22: 2577–2637.
25. Vögeli, B., J. Ying, A. Grishaev, and A. Bax. 2007. Limits on variations in protein backbone dynamics from precise measurements of scalar couplings. *J Am Chem Soc*. 129: 9377–9385.
26. Roche, J., Y. Shen, J.H. Lee, J. Ying, and A. Bax. 2016. Monomeric Aβ1–40 and Aβ1–42 peptides in solution adopt very similar Ramachandran map distributions that closely resemble random coil. *Biochemistry*. 55: 762–775.
27. Shen, Y., and A. Bax. 2010. SPARTA+: A modest improvement in empirical NMR chemical shift prediction by means of an artificial neural network. *J Biomol NMR*. 48: 13–22.
28. Kjaergaard, M., S. Brander, and F.M. Poulsen. 2011. Random coil chemical shift for intrinsically disordered proteins: Effects of temperature and pH. *J Biomol NMR*. 49: 139–149.
29. Kjaergaard, M., and F.M. Poulsen. 2011. Sequence correction of random coil chemical shifts: Correlation between neighbor correction factors and changes in the Ramachandran distribution. *J Biomol NMR*. 50: 157–165.

30. Hofmann, H., A. Soranno, A. Borgia, K. Gast, D. Nettels, and B. Schuler. 2012. Polymer scaling laws of unfolded and intrinsically disordered proteins quantified with single-molecule spectroscopy. *Proc Natl Acad Sci U S A*. 109: 16155–16160.

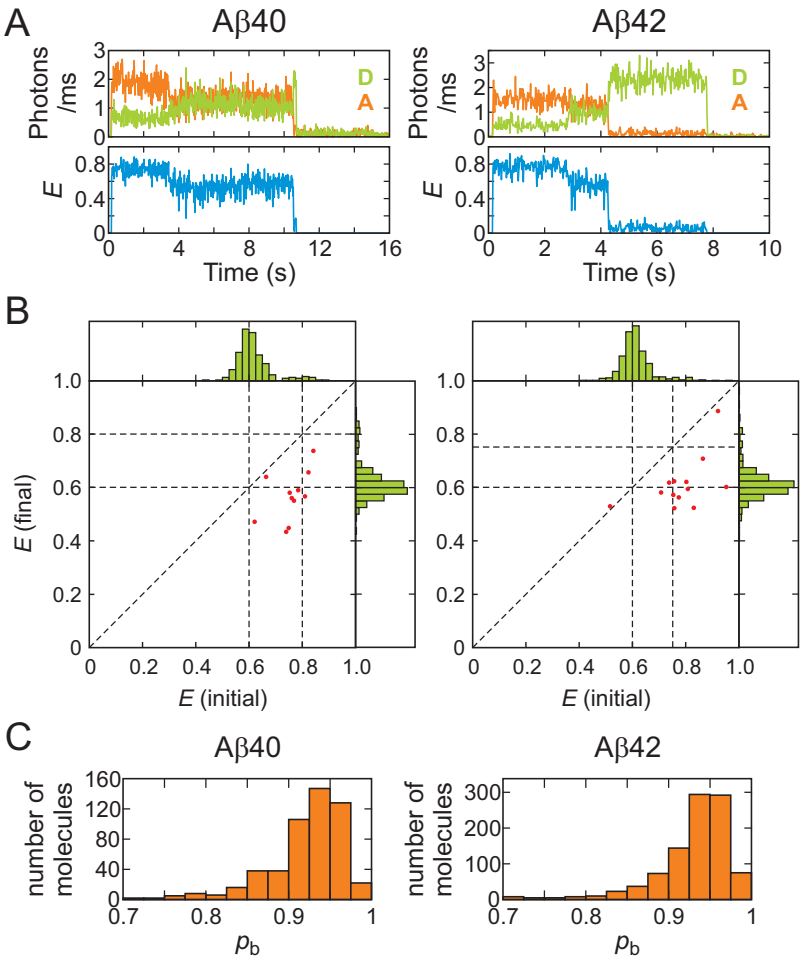

Figure S1. Alexa 647 photophysics. (*A*) Trajectories exhibiting FRET efficiency changes from $E \sim 0.8$ to $E \sim 0.6$. (*B*) Transition maps show that the transitions are localized on the lower right side of the diagonal, indicating that these transitions are irreversible on the time scale of tens of seconds. Similar irreversible transitions have been observed and attributed to the changes in the extinction coefficient of Alexa 647 (6). (*C*) The distribution of the acceptor bright state population extracted from the data in Fig. 4 using the maximum likelihood method with the 1-state acceptor blinking model.

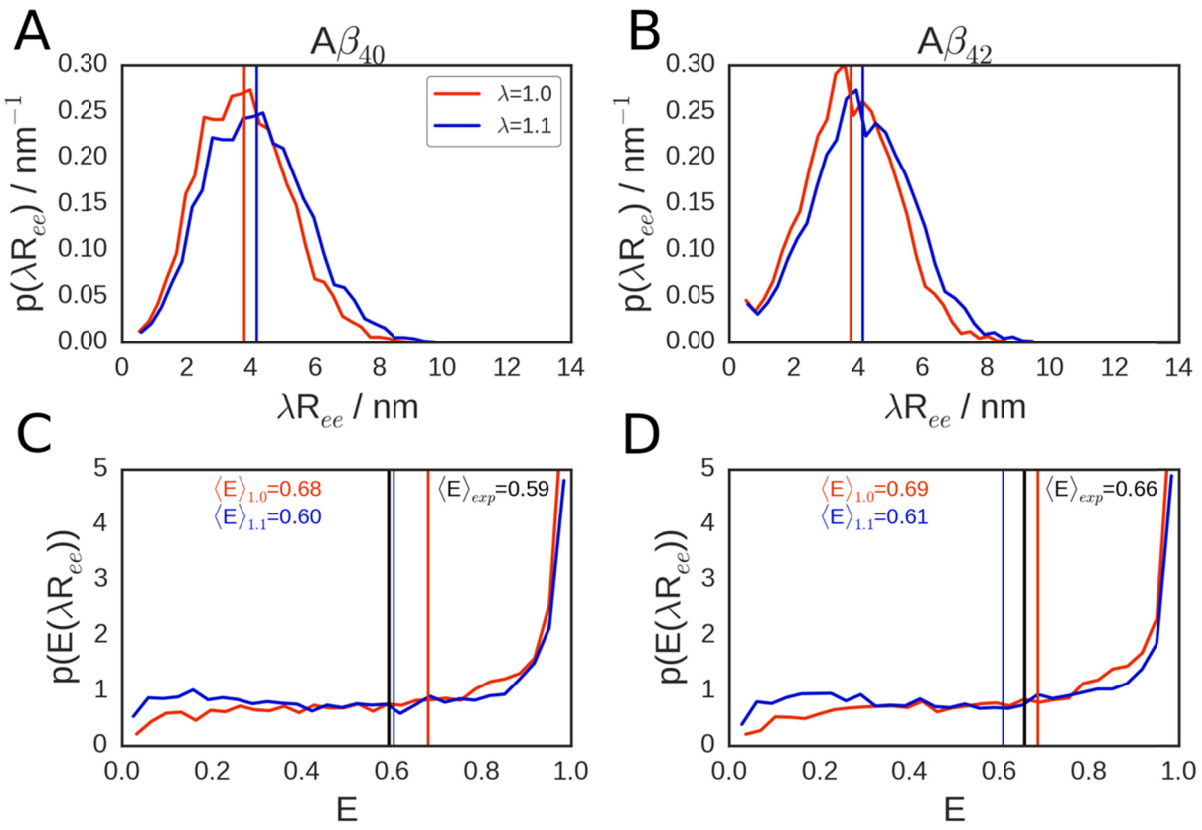

Figure S2. Sensitivity of FRET parameters to end-to-end distance distributions. For both Aβ40 (left) and Aβ42 (right), (*A*, *B*) scaling length scale for the end-to-end distance probability densities obtained from simulation (red) by a factor of 1.1 (blue) results in (*C*, *D*) FRET efficiency distributions whose means (colored vertical lines) are similar to or slightly smaller than the experimentally determined values (black vertical lines) for the freely diffusing peptides. Thus a shift of the distances of less than 10% would be sufficient to match the experimental distribution.

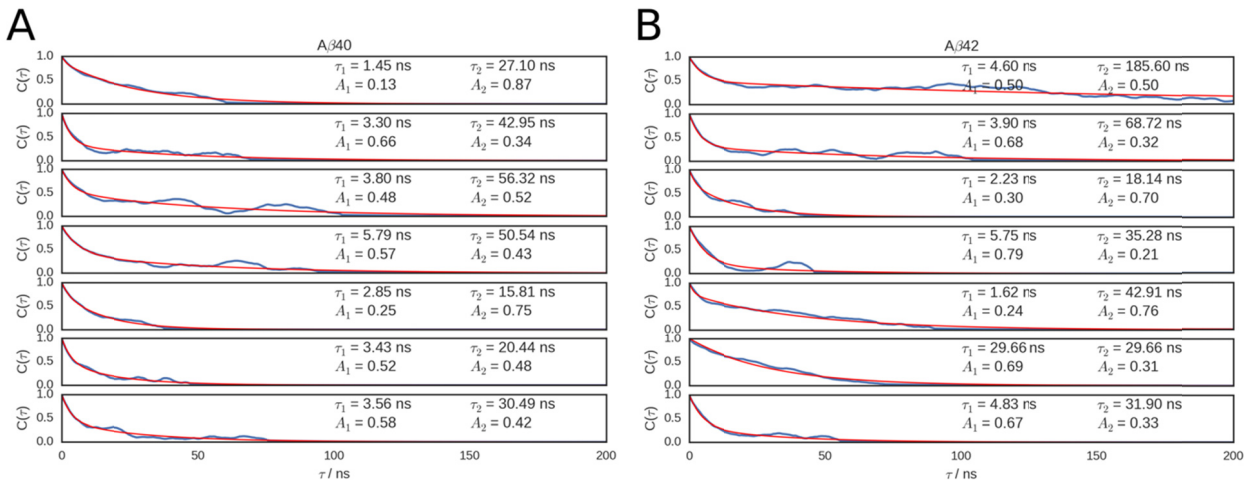

Figure S3. FRET efficiency autocorrelation functions $C(\tau)$ for simulations of dye-labelled Aβ40 (*A*) and Aβ42 (*B*), for each of the seven replicates, excluding the first 200 ns of data as equilibration. Blue curves are data and red are biexponential fits, with insets showing the fit results for decay times (τ_i) and exponential amplitudes (A_i). Averaging gives decay times of $\langle \tau_1 \rangle$ = 3.5 ± 0.5 ns (8 ± 3 ns) and $\langle \tau_2 \rangle$ = 35 ± 5 ns (60 ± 20 ns) for Aβ40 (Aβ42). The slow decay time is in quantitative agreement with the reconfiguration time determined from FRET experiments.

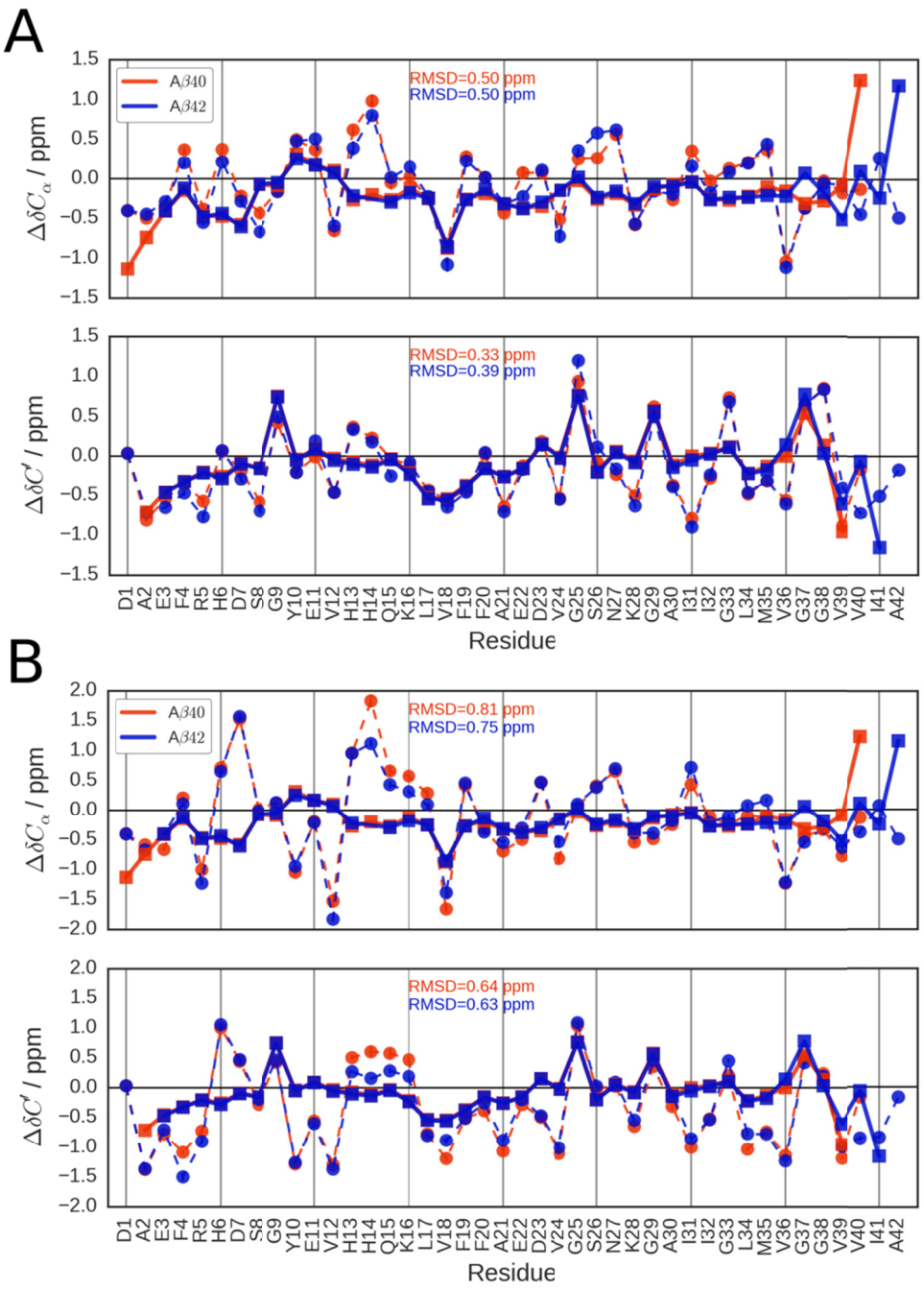

Figure S4. Comparison of secondary carbon chemical shifts between simulation (277 K) and experiment (26) with (*A*) Amber ff99SBws and (*B*) Amber ff03ws force fields. Simulation results are in circles and dashed lines while experimental results are in squares and thick solid lines. The shifts are relative to predicted random coil values. The root-mean-squared deviation, RMSD, between predicted values from simulations and experimental values are overlain, with results showing an agreement closer than the precision of shift prediction algorithm (see the text).

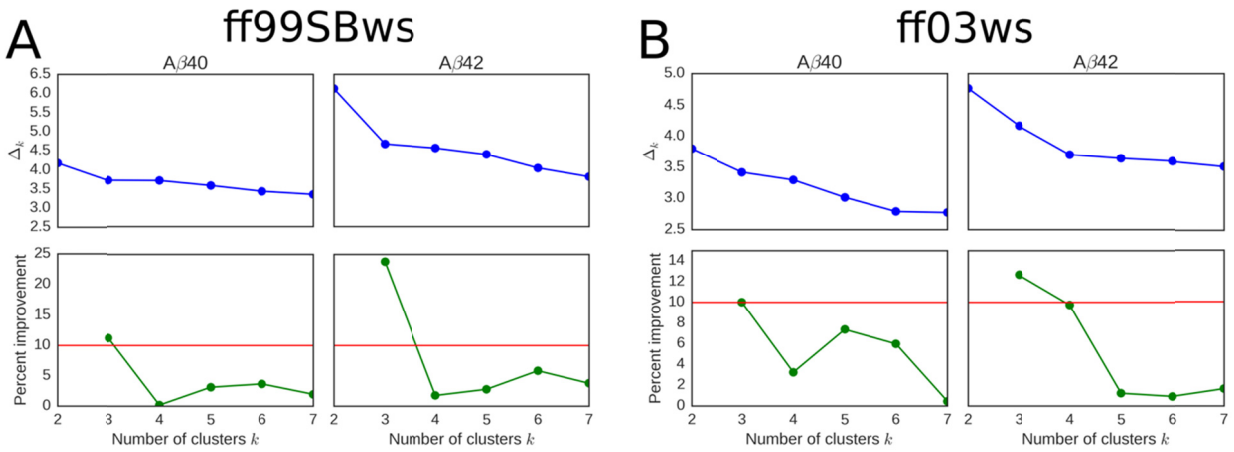

Figure S5. Determination of the number of clusters needed to describe the structural ensemble of (left column) Aβ40 and (right column) Aβ42 using the (*A*) Amber ff99SBws and (*B*) Amber ff03ws force field. Percent improvement in adding the k^{th} cluster is defined as $100 \times |\Delta_k - \Delta_{k-1}| / \Delta_2$, which measures the fractional improvement in capturing the ensemble-averaged contact map when an extra cluster center is added, relative to using only two clusters. In all cases, using more than three clusters results in insignificant (< 10%) improvement in describing the ensemble and comes at the cost of overfitting the data, save for the Aβ42 in Amber ff03ws, which requires four clusters.

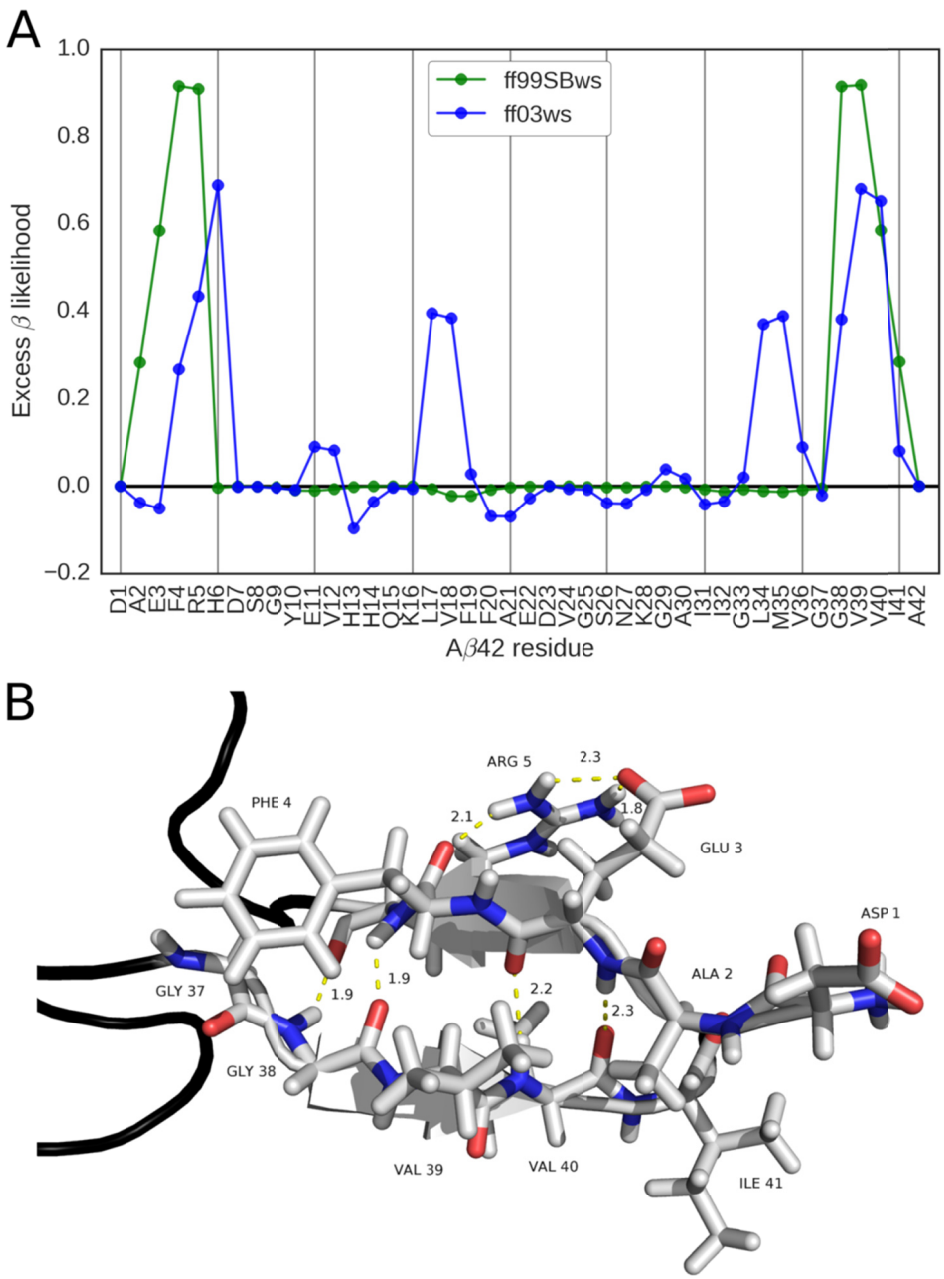

Figure S6. (*A*) Excess β-sheet likelihood, as defined in the SI section "Contact and cluster analysis", of the minor hairpin cluster of Aβ42 using the Amber ff99SBws and Amber ff03ws force fields. Both show significantly elevated propensity at the termini, demonstrating that these structures are true hairpins. (*B*) Terminal contacts of the Aβ42 hairpin conformation shown in Fig. 7(*D*). The hairpin is stabilized by hydrogen bonding between the backbone atoms of N-terminal residues 1 - 5 and C-terminal residues 38 - 41. Note that a similar structure for Aβ40 would be disfavored as the carboxyl group of the C-terminal V40 would be charged at physiological pH. The structure was made using PyMOL (Schrödinger, LLC), and the distances of the highlighted hydrogen bonds are in units of Angstroms.

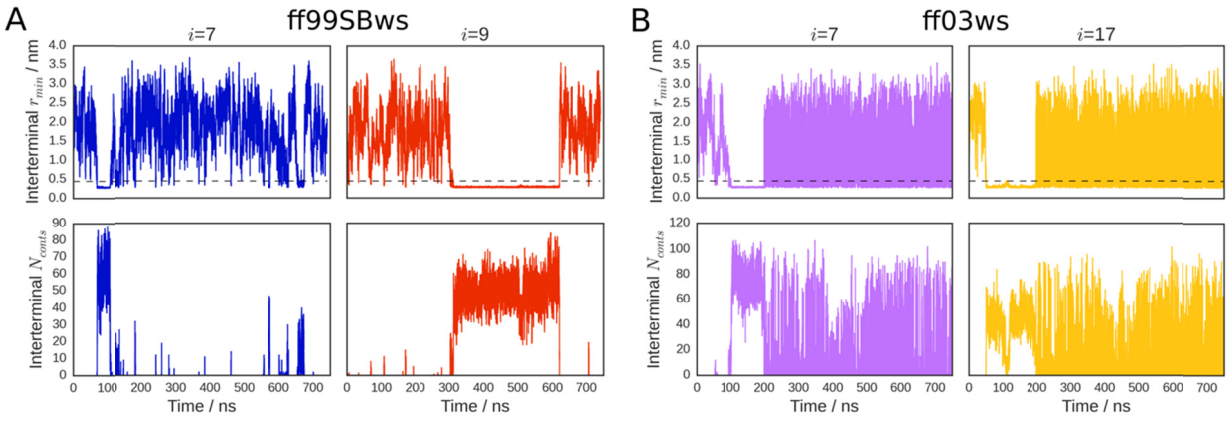

Figure S7. Reversibility of inter-terminal contacts. Minimum distance (top) and number of contacts (bottom) trajectories for the inter-terminal groups of Aβ42 in the Amber ff99SBws (*A*) and ff03ws (*B*) force fields, obtained from continuous REMD trajectories (i.e. followed through swaps in temperature space). Data are shown for only the two replicas with the highest contact population in each case, although other trajectories also showed contacts. As the observed contact maps of the minor hairpin clusters showed a small difference in contacting residues for each force field (see Figures 7(*D*) and S3(*D*)), we employed the following definitions of N- and C-termini: residues 2-5 and 38-41 for ff99SBws and residues 3-6 and 38-41 for 03ws.

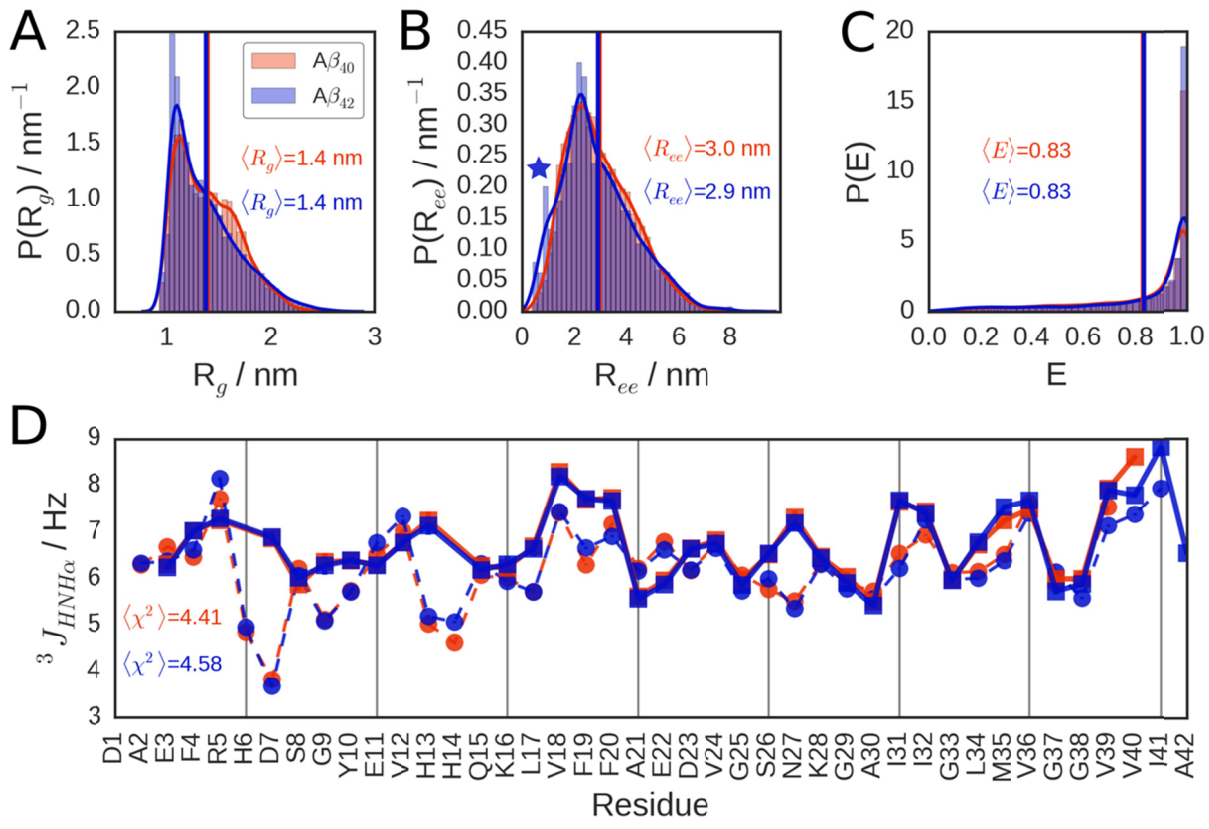

Figure S8. Ensemble observables for Aβ40 and Aβ42 using the Amber ff03ws force field. The results are consistent with the Amber ff99SBws results shown in Fig. 6.

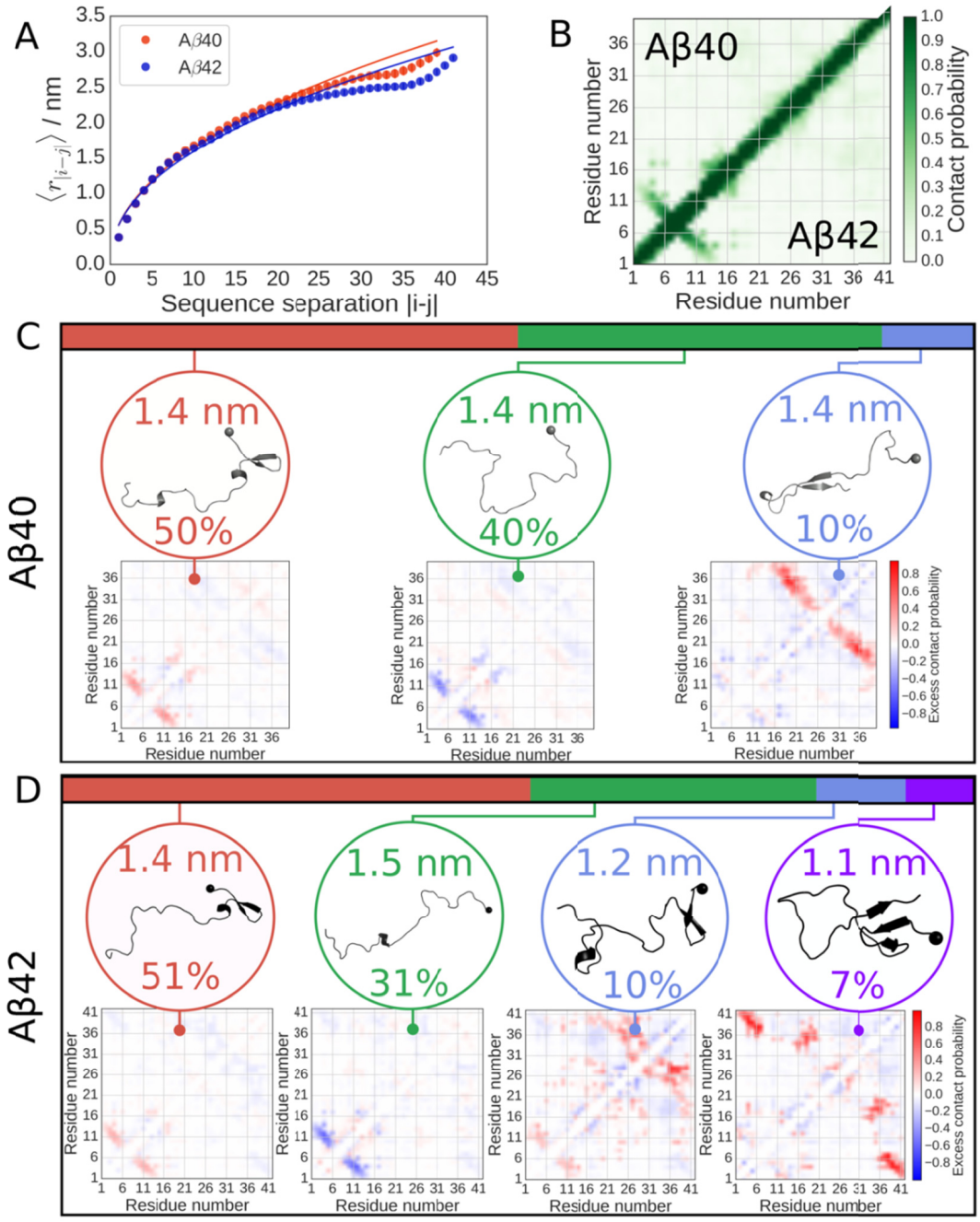

Figure S9. Conformational ensembles of Aβ40 and Aβ42 using the Amber ff03ws force field showing (*A*) internal Cα atom distance scalings for each peptide, with data shown as circles, and fits to a power law as described in the SI as solid lines, giving scaling exponents of ν = 0.4764 ± 0.0007 and 0.4625 ± 0.0006 respectively for Aβ40 and Aβ42. Also shown are the ensemble-averaged intramolecular contact maps (*B*) and cluster-averaged contact maps and most representative structures for Aβ40 (*C*) and Aβ42 (*D*). The results are consistent with the amber ff99SBws results shown in Fig. 7, save for significant population of hairpin structure in the N-terminal region for both peptides. Importantly, a hairpin formed by terminal contacts appears in the smallest cluster of the Aβ42 ensemble, as observed with Amber ff99SBws.

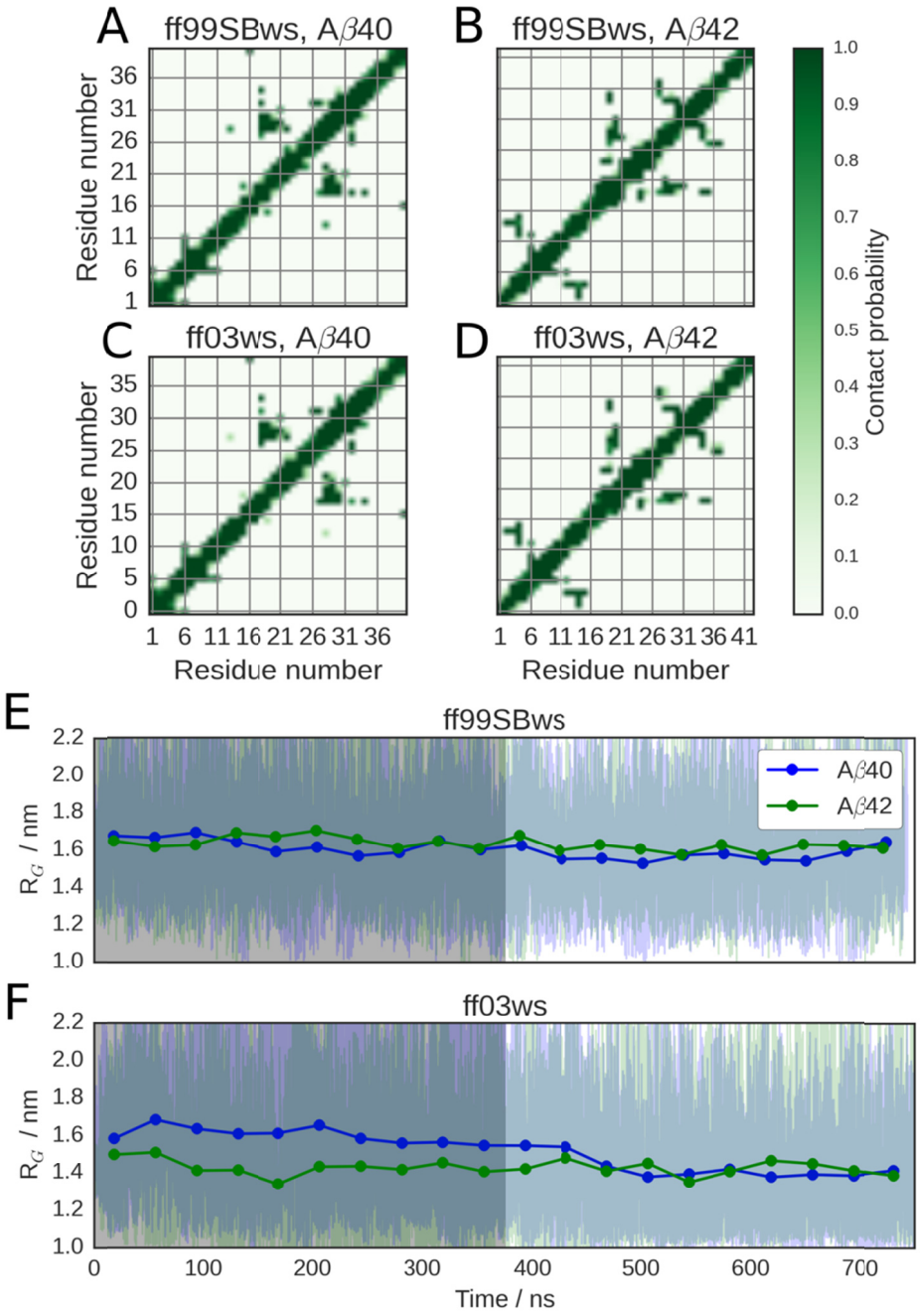

Figure S10. Initial configurations for Amber ff99SBws (*A, B*) and Amber ff03ws (*C, D*) force field REMD simulations, for both Aβ40 (*A, C*) and Aβ42 *(B, D)* peptides. Time-series of the radius of gyration R_g for both peptide isoforms using Amber ff99SBws (*E*) and Amber ff03ws (*F*) force fields. Light lines are raw data, thick circles and lines are block averages by dividing the simulation into 20 equal blocks and the light gray area is the first half of each simulation discarded as NPT equilibration when there is still a systematic drift in at least one of the peptide/force field combinations. Data taken from the 299 K replica.

Table S1. Comparison of the FRET efficiencies of Aβ40 and Aβ42 measured in PBS, and computed from simulation.

Experiment/Simulation	Construct	Aβ40	Aβ42
Free Diffusion[a]	Aβ	0.592 (± 0.005)	0.658 (± 0.002)
	Avi-Aβ	0.560 (± 0.005)	0.583 (± 0.004)
Immobilization (CW excitation)[b]	Avi-Aβ	0.572 (± 0.001)	0.581 (± 0.001)
Immobilization (Pulsed excitation)[c]	Avi-Aβ	0.600 (± 0.002)	0.604 (± 0.002)
Amber ff99SBws (implicit dyes)	Aβ	0.68 (± 0.01)	0.69 (± 0.01)
Amber ff99SBws (explicit dyes)	Aβ	0.75 (± 0.02)	0.79 (± 0.02)
Amber ff03ws (implicit dyes)	Aβ	0.83 (± 0.01)	0.833 (± 0.006)

[a] Errors are standard deviations obtained from the fitting of the FRET efficiency histograms in Fig. 2 to the Gaussian function. FRET efficiencies were corrected for background, donor leak, and γ-factor.

[b] Errors are standard deviations obtained from the diagonal elements of the covariance matrix calculated from the likelihood function (1-state with acceptor blinking) in Table S2. FRET efficiencies were corrected for background, donor leak, γ-factor, direct acceptor excitation, and acceptor blinking.

[c] Errors are standard deviations obtained from the fitting of the FRET efficiency histograms in Fig. 4B to the Gaussian function. FRET efficiencies were corrected for background, donor leak, γ-factor, direct acceptor excitation, and acceptor blinking.

Table S2. Maximum likelihood analysis parameters.[a]

Model	Parameters	Aβ40	Aβ42
2-state	E_1	0.598 (± 0.001)	0.614 (± 0.001)
	E_2	0.133 (± 0.004)	0.134 (± 0.004)
	k / ms^{-1}	12.2 (± 0.3)	14.1 (± 0.4)
	p_1	0.935 (± 0.002)	0.937 (± 0.002)
1-state with acceptor blinking	E	0.592 (± 0.001)	0.608 (± 0.001)
	k_b / ms^{-1}	11.7 (± 0.3)	13.1 (± 0.4)
	p_b	0.942 (± 0.001)	0.949 (± 0.001)
Donor-acceptor cross-correlation	k / ms^{-1}	15.3 (± 2.9)	16.5 (± 4.5)

[a] Errors are standard deviations obtained from the diagonal elements of the covariance matrix calculated from the likelihood function. The extracted FRET efficiencies are uncorrected values (apparent FRET efficiencies).

Table S3. Effect of excluding frames in which dyes (explicit dye simulations) or termini (implicit dye simulations) are in contact, for several definitions of contact cutoff. Contacts are defined as the minimum distance between any pair of heavy atoms, one from each contacting group.

Amber ff99SBws, explicit dyes				
	No exclusions	Exclude ≤ 0.45 nm	Exclude ≤ 0.75 nm	Exclude ≤ 1.0 nm
$\langle E \rangle_{A\beta40}$	0.75 ± 0.02	0.75 ± 0.02	0.75 ± 0.02	0.74 ± 0.02
$\langle E \rangle_{A\beta42}$	0.79 ± 0.02	0.78 ± 0.02	0.77 ± 0.02	0.77 ± 0.02
Amber ff99SBws, implicit dyes				
	No exclusions	Exclude ≤ 0.45 nm	Exclude ≤ 0.75 nm	Exclude ≤ 1.0 nm
$\langle E \rangle_{A\beta40}$	0.68 ± 0.01	0.68 ± 0.01	0.68 ± 0.01	0.68 ± 0.01
$\langle E \rangle_{A\beta42}$	0.69 ± 0.01	0.69 ± 0.01	0.682 ± 0.009	0.680 ± 0.009

Table S4. Reproducibility of *k*-means clustering, as measured by cluster-specific conditional probabilities of frame assignment overlap $p_k(\in 2 \mid \in 1)$ and $p_k(\in 1 \mid \in 2)$, as well as by average contact map distance $\|C_1, C_2\|_k$ between clusters.

Amber ff99SBws						
	Aβ40			Aβ42		
k	$p_k(\in 2 \mid \in 1)$	$p_k(\in 1 \mid \in 2)$	$\|C_1, C_2\|_k$	$p_k(\in 2 \mid \in 1)$	$p_k(\in 1 \mid \in 2)$	$\|C_1, C_2\|_k$
1	1.000	0.978	0.102	0.999	0.998	0.010
2	0.942	1.000	0.270	0.994	0.996	0.027
3	1.000	1.000	0.000	1.000	1.000	0.000
Amber ff03ws						
	Aβ40			Aβ42		
k	$p_k(\in 2 \mid \in 1)$	$p_k(\in 1 \mid \in 2)$	$\|C_1, C_2\|_k$	$p_k(\in 2 \mid \in 1)$	$p_k(\in 1 \mid \in 2)$	$\|C_1, C_2\|_k$
1	1.000	0.999	0.004	1.000	0.996	0.035
2	0.999	1.000	0.006	0.993	1.000	0.059
3	1.000	1.000	0.000	1.000	1.000	0.000
4	–	–	–	1.000	1.000	0.000